Mechanical testing and fracture analyses of miniaturized ZnO-based multilayer components

K. Macurova[1], M. Gruber[1], M. Pletz[1,2], P. Supancic[1,3], R. Danzer[1], F. Aldrian[4], R. Bermejo[1,γ]
[1] Institut für Struktur- und Funktionskeramik, Montanuniversitaet Leoben, [2] Department of Polymer Engineering and Science, Montanuniversitaet Leoben, [3] Materials Center Leoben Forschung GmbH, [4] TDK-EPC
[1]Franz-Josef-Straße 18,
A-8700 Leoben
Ph: +43-384-240-241-15; Fax: +43-384-240-241-02
[γ] *Corresponding author's* e-mail address: raul.bermejo@unileoben.ac.at

Abstract

Functional components are commonly fabricated combining a ceramic substrate with external and/or internal metallization (e.g. metal electrodes, vias, contact pads, etc.) using a tape casting process. Different layers are printed and/or fired (e.g. up to 800°C) onto the ceramic part to provide the component with a (certain) functionality. As a result of the combination of different materials (e.g. ceramic, glass, metal alloys) with different coefficients of thermal expansion, internal stresses may arise during the different fabrication steps. Although some of these tensile residual stresses may relax due to plastic deformation of metallic materials, stress concentrations generated in material junctions or terminations (imposed by geometrical constrains) may lead to cracks and/or reduce the component strength.

In this work different architectures combining metal and glass layers on the surface of ZnO substrates were investigated experimentally and numerically in order to identify weak points in commercial components. Mechanical testing using three-point-bending was performed on samples taken after different steps. A FE model was developed to (i) calculate residual stresses generated during the manufacturing process, and (ii) simulate the propagation of initial crack/defect during manufacturing. Experimental results were compared with numerical predictions. These results in combination with fractographic analyses were used to validate the finite element model in order to assess location of failure.

Key words

Functional ceramic components, miniaturized mechanical testing, crack propagation, FE modelling.

I. Introduction

Many applications in microelectronics involve combinations of ceramic and metal constituents. Functional components such as multilayer varistors (MLV), piezoelectric actuators (MPA), multilayer ceramic capacitors (MLCC), Low Temperature Co-fired Ceramics (LTCC) and semiconductors, among others, are examples of combination of a ceramic-based (or silicon based) substrate with internal electrodes as well as surface features (e.g. metallization, contacting pads, cylindrical vias, etc.) This combination of materials provides the component (or system) with certain functionality. Typical components are based on low temperature co-fired ceramics substrates (e.g. alumina-glass composites, ZnO), which enable the co-sintering of (low melting point) glass ceramics with high electrical conductivity materials (e.g. silver, gold, galvanized nickel). In the co-sintering process, different layers are printed and/or sintered (e.g. up to 800°C) onto the ceramic substrate according to the component design. Due to the different properties of the materials involved (e.g. thermal expansion coefficients (CTE), elastic constants, yield strength), internal stresses can develop in components during fabrication, which may induce cracks that truncate the electrical performance of the component [1], [2]. Although some of these tensile residual stresses may relax due to plastic deformation of metallic materials, stress concentrations generated in material junctions or terminations (imposed by geometrical constrains) may lead to failure during fabrication or in service.

In this work the structural integrity of ZnO-based multilayer components has been investigated combining experimental and numerical methods. Different architectures combining metal and glass layers on the surface of ZnO substrates were tested under three-point bending, and compared to bulk ZnO material. In order to identify the failure origin in the components, fractographic analyses were performed on broken samples. In addition, numerical simulations were carried out to understand the

effect of geometry and processing steps on arising residual stresses in the component. The numerical results were validated with cross-sections to reveal the onset of damage after the fabrication process. The implemented numerical model can be used to explain different mechanical behavior, predict critical configurations and can therefore help improving the reliability of ceramic-based functional components.

II. Investigated components

The investigated components are miniaturized ZnO-based thermo-elements for socket diodes, hereafter referred to as TESD, which are employed in microelectronic applications to serve as heat-dissipating substrates. This is attained by sintering of through-thickness vias and inner metallization layers in the ZnO substrate.

The investigated components are carriers for LEDs. Compared to conventional LED carriers like Al_2O_3 or AlN, ZnO based substrates provide an integrated ESD protection. The ESD protection inherent in the ZnO substrate eliminates the external ESD protection device, the landing area needed for this ESD component, all manufacturing and testing processes needed for the external protection device and the interference of the light radiation. With this solution a chip size package with integrated ESD protection for LEDs can be achieved.

A. Component geometry

Figure 1 schematically shows the typical build-up of a TESD component. It consists of a ZnO substrate (green), a silver metallization (light blue), a glass layer (blue) and a nickel (Ni) galvanic coating (orange). The typical dimensions of such TESD components are given in Fig. 1a. A detail of the cross-section of the component is shown in Fig. 1b. It is worth pointing out that the overlapping of the two metallization layers (i.e. M1 and M2) can be done following two distinct configurations. In configuration 1 (referred to as ***Conf. 1***) the area covered by the metallization 1 (M1) is larger than that of metallization 2 (M2), see Fig. 1c. In configuration 2 (named as ***Conf. 2***) the area metallization 2 (M2) is the one covering a larger area, see Fig. 1d.

B. Manufacturing process

For both configurations, after the tape cast processing of the ZnO substrate with internal electrodes and vias, the TESD is produced following these fabrication steps: (i) first metallization of silver (M1) onto the ZnO substrate, (ii) printing of a glass layer, (iii) second metallization of silver (M2) onto the top of M1 and the glass layer, and (iv) galvanization of the electroless nickel on the metallization M2, see top (orange) layer in Fig. 1. A schematic of the processing temperatures during the sintering and galvanization process are plotted in Fig. 2. It is important to highlight that only TESD components after the galvanization process (i.e. the end step) were tested and compared to ZnO bulk material.

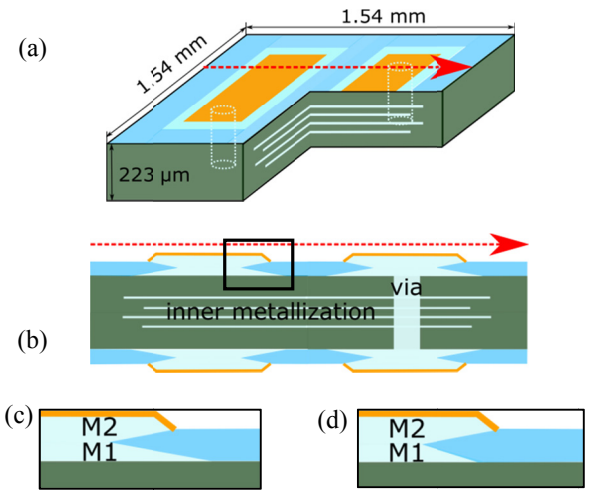

Fig 1: (a) 3D schematic of the TESD component, (b) Structure of the TESD, (c) Metallization configuration 1 (***Conf. 1***), (d) Metallization configuration 2 (***Conf. 2***).

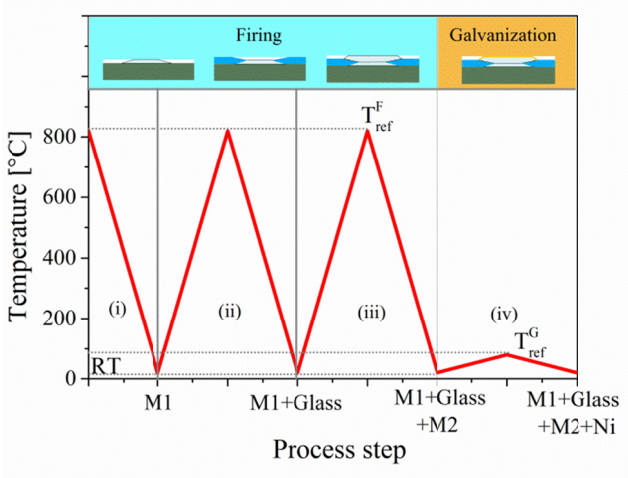

Fig 2: Temperature profile according to manufacturing process steps during firing and galvanization processes.

II. Mechanical characterization

A. Testing samples

Due to the small size of the TESD components (i.e. approx. 1.5 x 1.5 x 0.25 mm^3), bending bars were fabricated for the mechanical testing, containing equally spaced distributed TESD components corresponding to ***Conf. 1*** and ***Conf. 2***, see Figs. 3a and 3b, respectively. As a result, typical bending bars with dimensions (*b* x *t* x *l*)

3.8 mm x ~0.25 mm x 25 mm, were produced, with b, t and l being the width, thickness and length of the specimen, respectively.

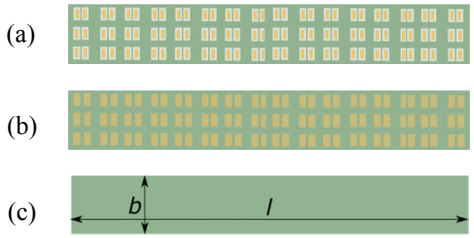

Fig 3: Rectangular bending bars containing (a) TESD ***Conf. 1***, (b) TESD ***Conf. 2***, and (c) bulk ZnO.

B. Strength evaluation: Weibull analysis

The bending tests were performed according to the ASTM C1161 standard [3] using a three-point bend (3PB) fixture, with an outer span S_0 of 20 mm. Tests were conducted in ambient conditions (25 °C, 15 % relative humidity) under displacement control at a rate of 5 mm/min using a universal testing machine (Zwick Z010, Zwick/Roell, Ulm, Germany) with a load cell of 200 N. The failure stress, σ_f, was calculated following the expression [3]:

$$\sigma_f = \frac{3}{2}\frac{PS_0}{bt^2}, \qquad (1)$$

where P is the fracture load. The thickness t was considered to be the substrate thickness (t_s) for the bulk samples, and the thickness of substrate + glass layer for the TESD components.

The failure stress values obtained for the three samples were analyzed according to Weibull theory [4]. The resulting strength distributions for every sample are plotted in a Weibull diagram (see Fig. 4), where the probability of failure, F, is plotted versus the failure stress, σ_f (calculated for every specimen according to Eq. (1)). The full line represents the best fit to the failure stress data using the maximum likelihood method. The Weibull parameters σ_0 (characteristic failure stress) and m (Weibull modulus) of each sample were calculated according to EN-843-5 [5], and are given in Table 1, along with the 90% confidence intervals.

Table 1: Weibull parameters (σ_0, m) for ***Conf. 1***, ***Conf. 2*** and ZnO bulk samples. The corresponding 90 % confidence intervals are given in brackets.

Sample	σ_0 [MPa]	m
Bulk	235 (230 – 240)	17 (12 – 20)
Conf. 1	230 (226 – 234)	20 (15 – 24)
Conf. 2	134 (130 – 138)	11 (8 – 13)

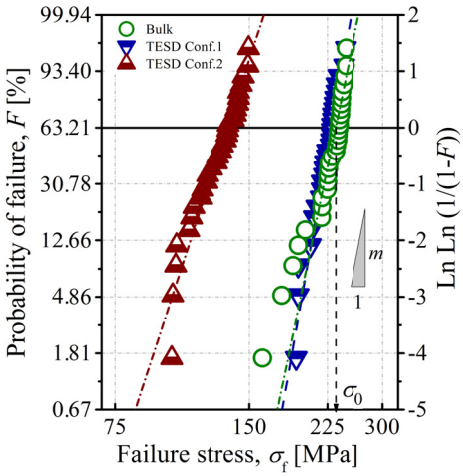

Fig 4: Weibull diagram showing the failure stress vs. probability of failure of TESD components under ***Conf. 1*** and ***Conf. 2***, and ZnO bulk material.

Fig. 4 shows that there is a significant difference in the failure stress values between ***Conf. 1*** and ***Conf. 2***, the former showing a similar strength distribution as the ZnO bulk sample. A failure analysis was performed aiming to explain these strength results.

C. Fractographic analyses

Cross-sections of selected fractured components corresponding to ***Conf. 1*** and ***Conf. 2*** are shown in Figs. 5a and 5b, respectively.

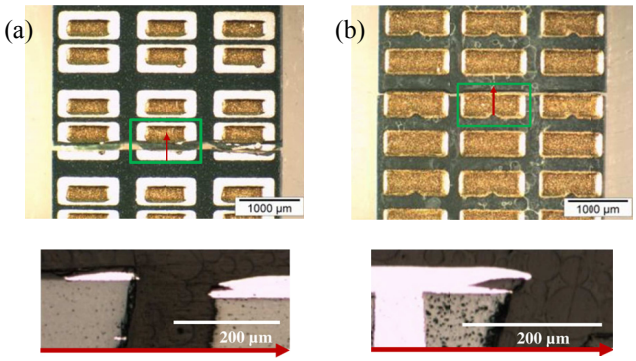

Fig 5: Cross sections of a TESD sample after 3PB for (a) ***Conf. 1*** and (b) ***Conf. 2***.

The cross-sections show that the component in ***Conf. 1*** seems to break through the silver metallization M1, whereas in ***Conf. 2*** the crack tends to propagate from M2 towards M1. Nevertheless, since the 3PB testing gives only information about failure of the whole component, the failure origin is not clearly observed in both cases. In order to understand the initiation of failure, a numerical analysis was developed.

IV. Numerical failure analysis

A. Numerical model

In order to explain the origin of failure of TESD, residual stresses arising in the component during its manufacturing should be calculated. Thus a parametric FE model was developed using the commercial software Ansys® [6] to (i) calculate residual stresses generated during cooling down from the maximum temperature of the corresponding process (see Fig. 2), and (ii) simulate the propagation of an initial crack/defect during manufacturing. To decrease calculation time, the TESD was modelled in 2D (the cross section) under the assumption of plane strain. The TESD geometry was simplified by neglecting the inner metallization layers and vias in the ZnO substrate, see Fig 6. Since only a thermal loading caused by the manufacturing process was applied, a half of the TESD component was analyzed with symmetric and periodic boundary conditions; see Fig. 5 (green frame) and 6. The model was discretized by 8-node quadratic elements. The area surrounded by a red dashed line in Fig. 6 was meshed with element size of 2 µm; the rest being meshed with element size of 10 µm. The dissimilar meshes were coupled using constraint equations. Geometrical parameters of the model are summarized in Table 2.

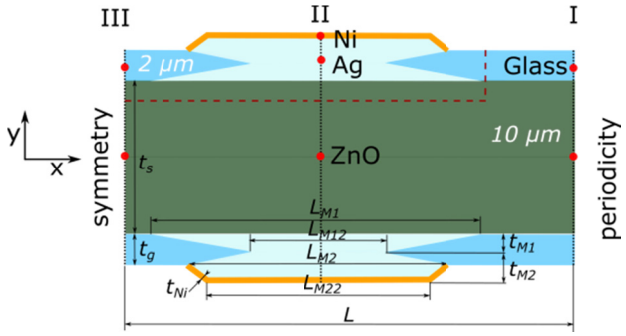

Fig 6: Details on the dimensions, boundary conditions and mesh size used for the numerical model.

Table 2: FEA model dimensions

Conf.	*1*	*2*		*1 & 2*	
L [mm]	0.77		t_s	[µm]	223
L_{M1} [mm]	0.32	0.28	t_g	[µm]	13.5
L_{M2} [mm]	0.3		t_{Ni}	[µm]	2.0
L_{M12} [mm]	0.196		t_{M1}	[µm]	6.75
L_{M22} [mm]	0.26		t_{M2}	[µm]	10.8

The material properties used in the FE model are summarized in Table 3. The silver plasticity was included in the model; its stress-strain curve was taken from literature [7] and implemented into FEA as a true stress – strain data points using a general multilinear kinematic model [6]. All other materials were modelled as linear-elastic. The reference temperature T_{ref} (stress-free state) was set according to the conditions of sintering (B) and galvanization (Ni) process, see Fig. 2. Intrinsic stresses developing in the nickel during galvanization due to chemical processes (crystallization, etc.) [8] were included in the model by implementing an additional thermal strain of approx. 0.11% for the nickel in the galvanization cooling step.

Table 3: Material properties at room temperature (RT)

	ZnO	Silver [7]	Glass	Nickel
E [GPa]	110	6.3	64	160
ν	0.32	0.37	0.22	0.31
CTE [ppm/°C]	6.7	21.6	3.3	13.4
T_{ref} [°C]	820[F]	820[F]	820[F]	80[G]

[F] Firing; [G] Galvanization

B. Residual stress field in the component

A central part of the failure analysis is based on the estimation of the residual stresses arising in the component due to CTEs mismatch of utilized materials during manufacturing. In this regards, the whole manufacturing process was simulated using an "element kill/birth" technique (see Ref. [6] for more details). The component was modelled without any initial defect (crack). The residual stress σ_x is plotted in Fig. 7 at the end of step (iv), i.e. after galvanization step.

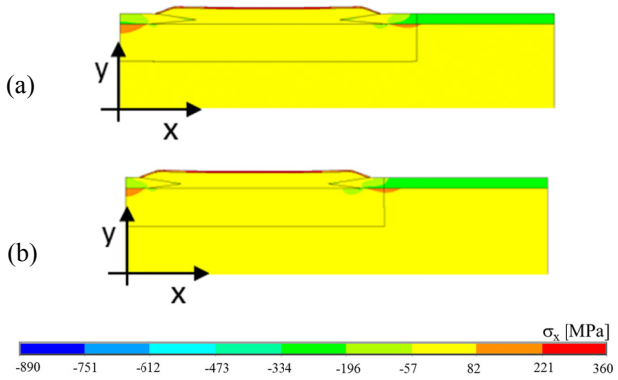

Fig 7: Residual stress σ_x [MPa] in the TESD after galvanization for (a) ***Conf. 1*** and (b) ***Conf. 2***.

Far from free edges the structure is subjected to an in-plane bi-axial stress state. The distribution of the in-plane residual stress σ_x was evaluated through the TESD thickness after galvanization step (iv) in locations I, II and III, see Fig. 6. Since ***Conf. 1*** differs from ***Conf. 2*** only in the length of the silver metallization M1, the stresses in location I and II are only slightly affected by M1. The stress values are evaluated in the middle of the material's layer thickness; see Fig. 6 (red points).

Table 1: FEA results of the stress σ_x [MPa] in locations I, II and III, i.e. in the middle of the material layer thickness.

	Location			
	I	**II**	**III**	
Conf.	***1 & 2***	***1 & 2***	***1***	***2***
Ni	-	+265	-	
Ag	-	+32	-	
Glass	–271	-	–181	–110
ZnO	+33	–7	–6	–10

Location I: FEA results show that the glass layer is under a constant compressive stress of –271 MPa and ZnO is under a constant tensile stress of +33 MPa, since CTE ZnO > CTE glass.

Locations II, III lay in the vicinity of the silver metallization electrode edges (M1, M2). The edge effects [9] significantly influence the residual stress distribution in those points. The stress is not constant over the material layer thickness.

Location II: Due to higher CTE of Ni and Ag in comparison to ZnO, tensile stresses are generated during cooling to RT in Ni with a value of +265 MPa and in Ag with value of +32 MPa. Besides, a high thermal shrinkage of Ni and Ag sets the ZnO substrate under compression, where σ_x reaches a value of –7 MPa.

Location III: in The tensile stress σ_x in glass in ***Conf. 1*** reaches –181 MPa, which is higher than that in ***Conf. 2*** reaching –110 MPa, due to ***Conf. 1*** M1 > ***Conf. 2*** M1. The stress level is lower than in location I because of Ag plasticity. The residual stress σ_x in ZnO is between –6 and –10 MPa for ***Conf. 1*** and ***2***.

Based on the residual stress analysis one can conclude that there is no significant difference between the stress state of ***Conf. 1*** and ***2***.

C. *Prospective crack propagation*

The second aim of the FE analysis was to determine a prospective direction of initial crack propagation due to manufacturing process. The crucial point was to identify the initial defect location, i.e. where the highest stress is concentrated. Based on the residual stress analysis, the stress concentration was observed in the material junction between nickel, silver and glass layers (thereafter called location **P**), as indicated in Fig. 8.

The nickel layer does not adhere sufficiently to the glass surface due to low adhesion between the glass and the nickel [10]. As a result, location **P** was assessed as a position of possible crack initiation.

In the stress-strain analysis, the location **P** represents a singularity problem due to a material junction in a combination with sharp edges (the nickel opening at the edge of the silver metallization M1 and the glass layer). Stress values of +171 MPa and +174 MPa in the vicinity of location **P** for ***Conf. 1*** and ***Conf. 2***, respectively, were obtained. It should be mentioned that the results are influenced by mesh size (here 2 µm); therefore the stress values in **P** should be assessed qualitatively rather than quantitatively.

In order to avoid a singularity problem in location **P**, an additional analysis introducing a crack with a size of 2 µm (i.e. a possible microstructural defect in the glass) was performed for both configurations. The direction of crack propagation was determined in terms of the crack angle φ in the glass, see Fig. 8. Since only small scale yielding develops in the linear-elastic glass, the stress intensity factor (K_I) concept, i.e. linear-elastic fracture mechanics, was used for the evaluation of crack propagation. In brittle, isotropic homogenous materials the crack growth is predicted to occur in direction of the highest K_I (tensile mode) [11].

The crack was modelled with its wake placed in location **P**, see Fig. 6. The FEA analysis was done for the TESD after galvanization, i.e. step (iv), as illustrated in Fig. 2. The residual stresses in the component were included by simulation of the whole manufacturing process. The stress singularity at the crack tip was treated using singularity elements [6]. The mesh surrounding the crack was refined by elements as small as 0.5 µm in size.

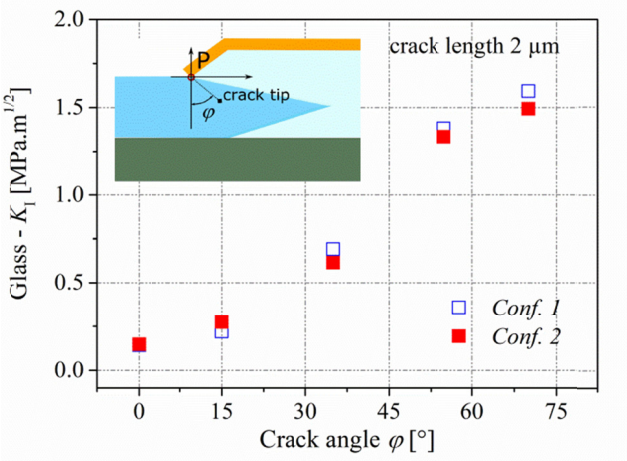

Fig 8: Stress intensity factor K_I in the glass as a function of the crack angle φ.

The results of the stress-strain analysis showed that high compressive stresses are generated in the glass, except in the vicinity of location **P**. This causes a maximum of K_I for cracks propagating near to the interface silver M1/glass, yielding an angle of *approx.* 83 ° (see Fig. 8).

It is shown that K_I exceeds the glass toughness (i.e. the crack propagates) only after galvanization. The fracture toughness of a borosilicate glass is *approx.* 0.8 MPa·m$^{1/2}$ [12]. The same trend is found for both configurations. K_I of

Conf. 1 does not differ significantly from K_I of ***Conf. 2***, corresponding to the stress state described in section *B*.

D. Fracture analysis validation

To determine the crack origin experimentally, focused ion beam (FIB) measurements were performed. For a better observation of the fracture, an area of *approx.* 10 x 25 µm^2 was cut out from unloaded samples in a location illustrated in Fig. 9a. The measurement was performed on TESD samples after the galvanization process. For both configurations it was observed that the interface silver M2/glass delaminates after galvanization (Fig. 9b), thus introducing a crack, which may trigger the fracture during bending. This finding agrees with the FE predictions on crack propagation near the interface (i.e. maximum K_I for large angles in Fig. 8). However it is not clear why the strength of ***Conf. 1*** and ***Conf. 2*** was significantly different (Fig. 4), despite similar initial delaminating cracks. In this regard, a further FE analysis should be carried out including a delaminating crack in the model and applying external bending to simulate the mechanical tests. Previous works from some of the authors showed the influence of metallization in arresting the propagation of initial cracks [13], [14]. This mechanism may also take place in the TESD ***Conf. 2*** samples studied here, thus avoiding the failure owed the starting delaminating crack. This will be investigated in future work combining in-situ FIB tests and numerical simulation of crack propagation in the TESD multilayer structure.

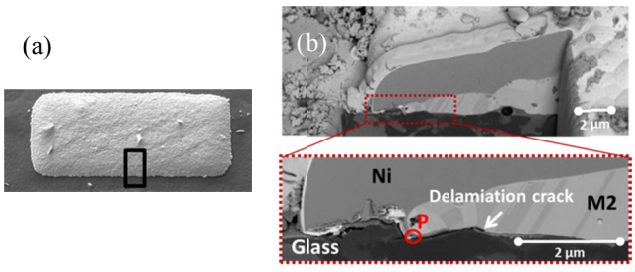

Fig 9: (a) FIB cut location, (b) ***Conf. 2***: Interface silver M2/glass delamination after galvanization.

V. Conclusions and outlook

The fracture behavior of miniaturized ZnO-based multilayer components was investigated under three-point bending on two architectures with different combination of metal and glass layers on the surface of ZnO substrates. In one case, a different strength distribution was found, as compared to bulk ZnO material. Fractographic analyses revealed different fracture patterns.

A FE analysis simulating the residual stress distribution during the fabrication process showed relatively high stress concentration in the junction between metal and glass layers. Such location was found to be the fracture origin in both configurations (i.e. crack initiation). A fracture mechanics analysis showed a preferred angle of crack propagation, being closed to the metal-glass interface, as confirmed with the fractography. Nevertheless, based on these results, the difference in strength between both configurations remains unclear. Further analyses of crack propagation should help to explain the effect of the underlying structure on such strength difference.

Acknowledgment

Financial support by the Austrian Federal Government (in particular from the Bundesministerium für Verkehr, Innovation und Technologie and the Bundesministerium für Wirtschaft, Familie und Jugend) represented by Österreichische Forschungsförderungsgesellschaft mbH and the Styrian and the Tyrolean Provincial Government, represented by Steirische Wirtschaftsförderungsgesellschaft mbH and Standortagentur Tirol, within the framework of the COMET Funding Programme is gratefully acknowledged.

References

[1] A. G. Evans, D. R. Biswas, and R. M. Fulrath, “Some Effects of Cavities on the Fracture of Ceramics: I, Cylindrical Cavities,” *J. Am. Ceram. Soc.,* vol. 62, no. 1-2, 1979. pp. 95-100

[2] C. H. Hsueh, and A. G. Evans, “Residual Stresses and Cracking in Metal/Ceramic Systems for Microelectronics Packaging,” *J. Am. Ceram. Soc.,* vol. 68, no. 3, 1985. pp. 120-127

[3] ASTM C 1161-02c, "Standard Test Methods for Flexural Strength of Advanced Ceramics at Ambient Temperature," ASTM C 1161-02c, American Society for Testing and Materials, 2002.

[4] W. Weibull, “A statistical distribution function of wide applicability,” *J. Appl. Mech.,* vol. 18, 1951. pp. 253

[5] EN 843-5, "Advanced Technical Ceramics - Monolithic Ceramics - Mechanical Tests at Room Temperature - Part 5: Statistical Analysis," *EN 843-5*, 1997, p. 40.

[6] ANSYS® Academic Research, “Release 14.5,”

[7] D.-j. Yu, X. Chen, G. Chen *et al.*, “Applying Anand model to low-temperature sintered nanoscale silver paste chip attachment,” *Materials & Design,* vol. 30, no. 10, 2009. pp. 4574-4579

[8] G. A. Di Bari, "Electrodeposition of Nickel," *Modern Electroplating*, pp. 79-114: John Wiley & Sons, Inc., 2010.

[9] F. D. Fischer, T. Antretter, and E. R. Oberaigner, “Mechanics of sheared bands – Applications to faults, twins and variants,” *Mechanics of Materials,* vol. 40, no. 4–5, 2008. pp. 195-205

[10] C. P. Miguel, "Electroless nickel plating on glass," Google Patents, 1972.

[11] T. L. Anderson, *Fracture Mechanics: Fundamentals and Applications*, 3rd ed., Orlando: CRC Press Inc., 2005.

[12] "www.matweb.com."

[13] M. Deluca, R. Bermejo, M. Pletz *et al.*, “Strength and fracture analysis of silicon-based components for embedding,” *J. Eur. Ceram. Soc.,* vol. 31, no. 4, 2011. pp. 549-558

[14] M. Deluca, R. Bermejo, M. Pletz *et al.*, “Influence of deposited metal structures on the failure mechanisms of silicon-based components,” *J. Eur. Ceram. Soc.,* vol. 32, no. 16, 2011. pp. 4371-4380